Stable, Conductive, Adhesive Polymer Patterning Inside a Microfluidic Chamber for Endothelial Cell Alignment

*Elena Mancinelli, Silvia Taccola, Ellen Slay, Chalmers Chi Cheng Chau, Nizzy James, Benjamin Johnson, Kevin Critchley, Russell Harris, and Virginia Pensabene**

Endothelial cells (ECs) line the inner walls of blood vessels, respond to shear stress by elongating in the direction of flow. Engineering aligned ECs in vitro is essential for modeling human vascular diseases and for drug testing. Current microfluidic approaches mainly rely on unidirectional laminar flow, uniform coating of surfaces to improve cellular adhesion or alteration of the surface topography. Challenges persist due to shear stress-induced changes in cellular behavior, especially in complex multicellular environments and the time needed for the cells to align and polarize inside the microfluidic conduits. Generally, protein coating processes and physical treatments are also not compatible with the steps required for the assembly of microfluidic devices. This approach employs aerosol jet printing (AJP) to precisely pattern poly(3,4-ethylenedioxythiophene) polystyrene sulphonate (PEDOT:PSS) within microfluidic chambers in a single step. It is shown that the PEDOT:PSS is biocompatible and facilitates EC adhesion, patterning, elongation, and alignment. Under capillary flow, the cells retain their pattern-induced morphology over 7 d, confirming the efficacy of the approach in promoting cellular organization, eliminating the need for external pumps. Furthermore, it is demonstrated that the PEDOT:PSS pattern retains structural integrity and electrical stability following oxygen plasma treatment, required for assembling of fully enclosed microfluidic devices.

1. Introduction

Living tissues sense and respond to mechanical, physical, and chemical extracellular cues.[1,2] In striated muscles, nerves, and blood vessels, these cues coordinate the alignment of local cell types.[3] Endothelial cells (ECs), lining vessel walls, maintain vascular homeostasis by aligning with the vessel axis along the direction of the blood flow-induced shear stress.[4] Altered EC alignment can indicate pathological vascular conditions like atherosclerosis[5] and a leaking endothelium unable to protect organs from blood-circulating toxins.[6] Thus, engineering a physiologically aligned endothelium in vitro is crucial not only for understanding vascular function, but also for disease progression and drug response.[7,8] Due to the link between flow and EC alignment, microphysiological systems (MPS) are commonly employed to induce cell alignment in vitro. MPS replicates

---

E. Mancinelli, E. Slay, C. C. C. Chau, V. Pensabene
School of Electronic and Electrical Engineering and Pollard Institute
University of Leeds
Leeds LS2 9JT, UK
E-mail: v.pensabene@leeds.ac.uk

E. Mancinelli, C. C. C. Chau, K. Critchley, V. Pensabene
Bragg Centre for Materials Research
University of Leeds
Leeds LS2 9JT, UK

S. Taccola, R. Harris
Future Manufacturing Processes Research Group
University of Leeds
Leeds LS2 9JT, UK

E. Slay, C. C. C. Chau
School of Molecular and Cellular Biology and Astbury Centre for Structural Molecular Biology
University of Leeds
Leeds LS2 9JT, UK

N. James, B. Johnson, K. Critchley
School of Physics and Astronomy
University of Leeds
Leeds LS2 9JT, UK

V. Pensabene
Faculty of Medicine and Health
Leeds Institute of Medical Research at St James' University Hospital
University of Leeds
Leeds LS2 9JT, UK

The ORCID identification number(s) for the author(s) of this article can be found under https://doi.org/10.1002/admt.202400404

DOI: 10.1002/admt.202400404

human organ or tissue structure and function on a micrometric scale, typically with microfluidic channels for cell culture under controlled flow conditions. Physiological shear stress sensed by ECs ranges from 2 to 20 dyne cm^{-1} in veins and arteries.[9] Recreating these stresses requires channels with dimensions from tens to hundreds of micrometers, achievable through soft-lithography, a microscale pattern fabrication method widely employed to fabricate microfluidic chambers for cell culture.[10] EC microfluidic culture and maintenance under continuous shear stress has become standard practice in cardiovascular studies.[11,12] and typical experimental protocols are based on the loading of endothelial cells into an ECM coated channel and the exposure to continuous flow for several hours (up to days) for the cells to polarize and to form a tight endothelium. Endothelialized microfluidic channels have found application in investigating neurovascular and neurodegenerative diseases,[13] renal filtration and absorption,[14] tumor metabolism and drug response,[15] and liver bile conduct.[16]

Despite its physiological relevance, perfused microfluidic endothelial culture introduces inherent challenges. If uncontrolled, shear stress may result in unforeseen alterations in cellular behavior and when coculturing ECs with other cell types, high shear stress can disturb neighboring cells.[17] A comparative study conducted on human umbilical vein endothelial cells (HUVECs) and lymphatic endothelial cells revealed diverse responses to the same shear stress values, leading to alignment loss and potential apoptotic reactions outside specific shear stress ranges.[18] Flow needs to be precisely tuned to prevent waste accumulation without diluting growth factors.[19,20] Computational models demonstrated that rapid, periodic medium changes are expected to preserve cell health, whereas continuous perfusion may exert detrimental effects.[21,22] Moreover, interconnecting microfluidic devices with off-chip systems, like syringes or peristaltic pumps, introduces complexity and requires additional electrical power for operating the pumps. Given these challenges, alternative techniques for cell alignment become essential, either as substitutes for shear stress or in conjunction with it.

Cells such as neurons[23] and cardiac muscle cells[24] align in response to electrical stimulation while reshaping ECs benefits more from topographical and chemical substrate modifications, mirroring the vascular extracellular matrix (ECM).[25–29] Narrow micropatterned adhesive protein strips induce EC alignment without flow,[30,31] but shear stress addition reduces apoptosis.[31]

To achieve this mutual integration, patterning methods and materials must align with gold-standard lithography techniques for MPS assembly. Devices made of poly(dimethyl siloxane) (PDMS), an elastomer extensively used for MPS fabrication, typically involves an oxygen plasma activation step for permanent bonding between different layers. Transferring protein patterns inside a microfluidic device often follow standard micro-contact printing. A PDMS stamp is used to transfer the liquid protein on a pre-plasma activated flat surface.[32–34] Alternatively, the flat surface can be pre-coated and etched selectively.[30] The patterned surface is then aligned and bonded with the microfluidic conduit. However, the wet patterned substrate interferes with the use of the vacuum chamber and the formation of the plasma. Additionally, the plasma treatment causes strong surface oxidation and handling and assembling steps lead to denaturation and dehydration of bio-derived, patterned, ECM proteins and other adhesive material (e.g., poly-L-lysine). In order to overcome this challenge, it is common practice, but not an efficient method, to cover the pattern before performing plasma activation for device bonding in order to preserve the protein nature.

Aerosol jet printing (AJP) is an emerging contactless direct-write technology with distinct advantages in terms of design flexibility, responsive production, wide ink compatibility, printing resolution of the order of 10 µm and large nozzle stand-off distance (1–5 mm).[35] For microscale deposition, this enables the manufacturing of high-resolution features on to various flat and 3D surfaces, different surface textures, across curved surfaces, and into channels.[36] Initially developed for the manufacture of electronic circuitry, more recently, AJP has been applied to a diverse range of applications, including high-resolution deposition of biological materials for cell patterning.[37–39]

Compared to other methods which enable the formation of cell patterns on homogeneous 2D substrates[40–42] the use of AJP technology presents several advantages. First, most of the standard patterning methods require multiple steps and combinational approaches that include template-based methods such as photolithography, microcontact printing and soft lithography.[43–46] These very complicated and labor-intensive methods significantly increase fabrication time and cost and are not amenable to adaptation and mass customization. In order to overcome these limitations, direct-write techniques such as inkjet and extrusion-based printing, have been used for the deposition of guidance cues[47] or the direct deposition of live cells.[48] However, these approaches can cause high mortality rates due to excessive forces on the cells during the ejection and are often limited by material selection and offer limited printing resolution.[48] Within this framework, AJP-based method represents a valid alternative for the digitally driven microscale deposition of chemical and topographical features. In particular, we have recently reported the use of AJP to reliably create microscale poly(3,4-ethylenedioxythiophene) polystyrene sulfonate (PEDOT:PSS) features on PDMS substrates; a combination which provides a respective attractive/nonattractive cell adhesion response.[49] We showed the capability to deposit complex patterns with different shaped designs on 2D PDMS surfaces, including curved lines, corners, and dots. The surface treatment invoked a controllable response in the adhesion of different cell lines and subsequent directionality of the cell growth according to the printed patterns.[41]

Significantly for microscale deposition, AJP can be used to pattern onto both planar and non-planar substrates owing to its large nozzle stand-off distance (≈5 mm) allowing for patterning over existing structures, different surface textures, across curved surfaces, and into channels.

PEDOT:PSS is known as a biocompatible, conductive polymer blend.[50] Due to its mechanical flexibility, transparency, and resistance against chemical and temperature changes, it has found large application as stretchable sensors,[51] electrodes for a variety of application in tissue engineering[52] and cellular monitoring in microfluidic devices.[53] It shows adjustable effects on cellular adhesion and contributes to vascular cell maintenance in vitro.[54]

In this study, we introduce a protocol for stable PEDOT:PSS patterning within a microfluidic chamber by utilizing AJP technology. We measure alignment of HUVECs, By Raman spectroscopy and atomic force microscopy we evaluate potential

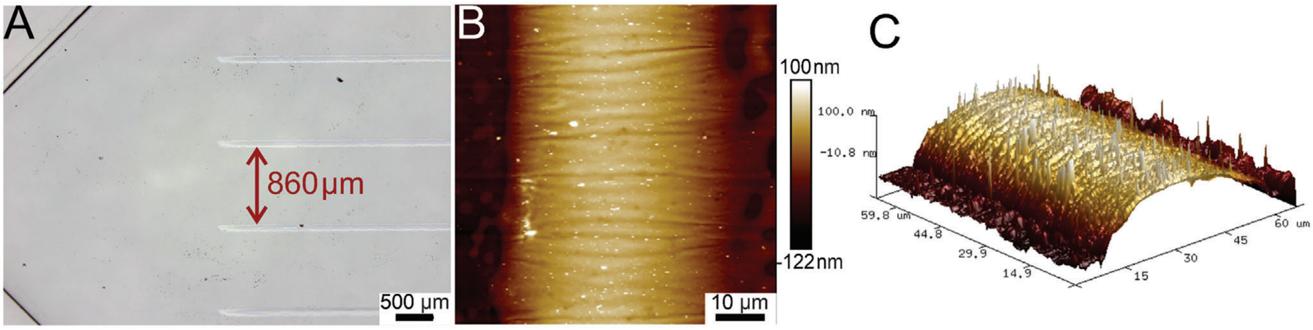

Figure 1. PEDOT:PSS aerosol jet printed pattern inside a microfluidic chamber: A) 6 parallel PEDOT:PSS lines spaced 860 µm, regularly distributed inside the chamber and aligned with the longest dimension of the chamber corresponding with the direction of the flow from inlet to outlet; AFM scan showing a PEDOT:PSS line with B) a thickness of 200 nm and C) a width of 50 µm (scale bars: A) 500 µm, B) 500 µm).

superficial and chemical characteristics of the PEDOT:PSS pattern on the PDMS, before and after exposure to oxygen plasma. We investigated the stability of the conductive patterns after device assembly. Finally, we quantify the alignment of the cells after seven days of culture under capillary flow and their adhesion on the patterned PEDOT:PSS.

2. Results and Discussion

2.1. PEDOT:PSS Pattern Printed by AJP Maintains Biocompatibility and Adhesive Strength for HUVECs in Microfluidic Devices with Prolonged Patterning Efficiency

The AJP deposition method facilitates the precise printing of ultrathin PEDOT:PSS patterns within micrometric PDMS chamber. Achieving an optimal pattern necessitates a careful combination of material formulation and printing parameters. The objective is to generate a pattern with a height significantly lower than the microfluidic chamber depth (100 µm), preserving fluid dynamics, and with a width sufficient to accommodate at least one entire cell. A series of parallel lines were printed to induce HUVECs alignment and elongation along the longest dimension of the tracks to mimic endothelial cell alignment along the longitudinal direction of the blood vessel. The lines were equally spaced to avoid altering cellular behavior within the chamber and strategically positioned far enough apart to allow successful cellular patterning. Fine movements of the stage during deposition enabled an interline space of <1 mm (860 µm) (**Figure** 1A). Printed lines reached a maximum thickness of around 100 nm (Figure 1B), three orders of magnitude below the chamber depth, and exhibit a parabolic shape with a width at base of approximately 50 µm (Figure 1C). This design allows for the accommodation of cobblestone-like HUVECs measuring 40 µm in diameter in vitro.[55]

The biocompatibility of PEDOT:PSS patterns, previously demonstrated with different cell types,[39] was reaffirmed here upon integration into a microfluidic device. After seven days of cell culture on PEDOT:PSS-patterned microfluidic chambers under capillary flow, the HUVECs on the patterns exhibit a viability of 75% ± 4% ($N = 9$ images across 3 devices, Figure S1 in Supporting Information). From 24 h post-seeding, actin filaments (F-actin) were observed in HUVECs cultured on plain PDMS substrates (**Figure** 2A), as well as under both static (Figure 2B) and capillary flow (Figure 2C) conditions within a PDMS microfabricated chamber patterned with PEDOT:PSS lines. Comparative analysis highlights the efficacy of the patterning, showing a homogeneous cell distribution on plain non-patterned PDMS (Figure 2A) and a distinct inclination for cells to proliferate along PEDOT:PSS lines (Figure 2B,C) when present. Under capillary flow conditions (Figure 2C), the cell proliferation was exclusively observed along PEDOT:PSS tracks and not on plain PDMS spaces. During the initial 24 h post-seeding, the number of attached cells showed no significant difference between static and capillary flow devices ($N = 9$ images across three devices). This was observed for both patterned areas (static: 68 ± 22 cells per mm^2, capillary flow: 82 ± 11 cells per mm^2) and plain PDMS areas between the lines (static: 71 ± 48, capillary flow: 49 ± 27) (see Figure S2 in Supporting Information). Interestingly, under the static condition, the PEDOT:PSS pattern provided limited guidance to the cells. When medium was retained on the PEDOT:PSS microfabricated substrates for 24 h, allowing cells to proliferate without refreshing, the entire area became covered by a confluent cell population after 7 d of culture (Figure 2B). The proliferation outside the patterned areas was around 2.5 times higher than in static devices compared to those under capillary flow (static: 84%, capillary flow: 34%) (Figure S2 in Supporting Information). Patterning efficiency, defined as the percentage of cells growing on pattern lines, significantly decreased from 52 ± 12% one day after seeding to 31 ± 3% at the seventh day of culture under static conditions ($N = 9$ images across 3 devices) (Figure S2 in Supporting Information). In capillary flow-exposed devices ($\tau_{\max} = 6$ dyne cm^{-2}), over 60% of cells concentrate in pattern areas by the seventh day of culture (62 ± 9%) (Figure S2 in Supporting Information). Cell adhesion to PEDOT:PSS remained robust after one week, resisting a flow rate of 500 µL min^{-1} for at least 30 min ($\tau = 8$ dyne cm^{-2}). Post-flow and a two-hour recovery at 37 °C and 5% CO$_2$, the cell count on PEDOT:PSS lines shows no significant difference ($N = 18$ images across three devices, Figure S3 in Supporting Information).

2.2. PEDOT:PSS Pattern Preserves Structural Integrity and Electrical Stability after Oxygen Plasma Activation

As shown in the previous section, PEDOT:PSS maintains adhesive properties post-integration into a fully enclosed microfluidic

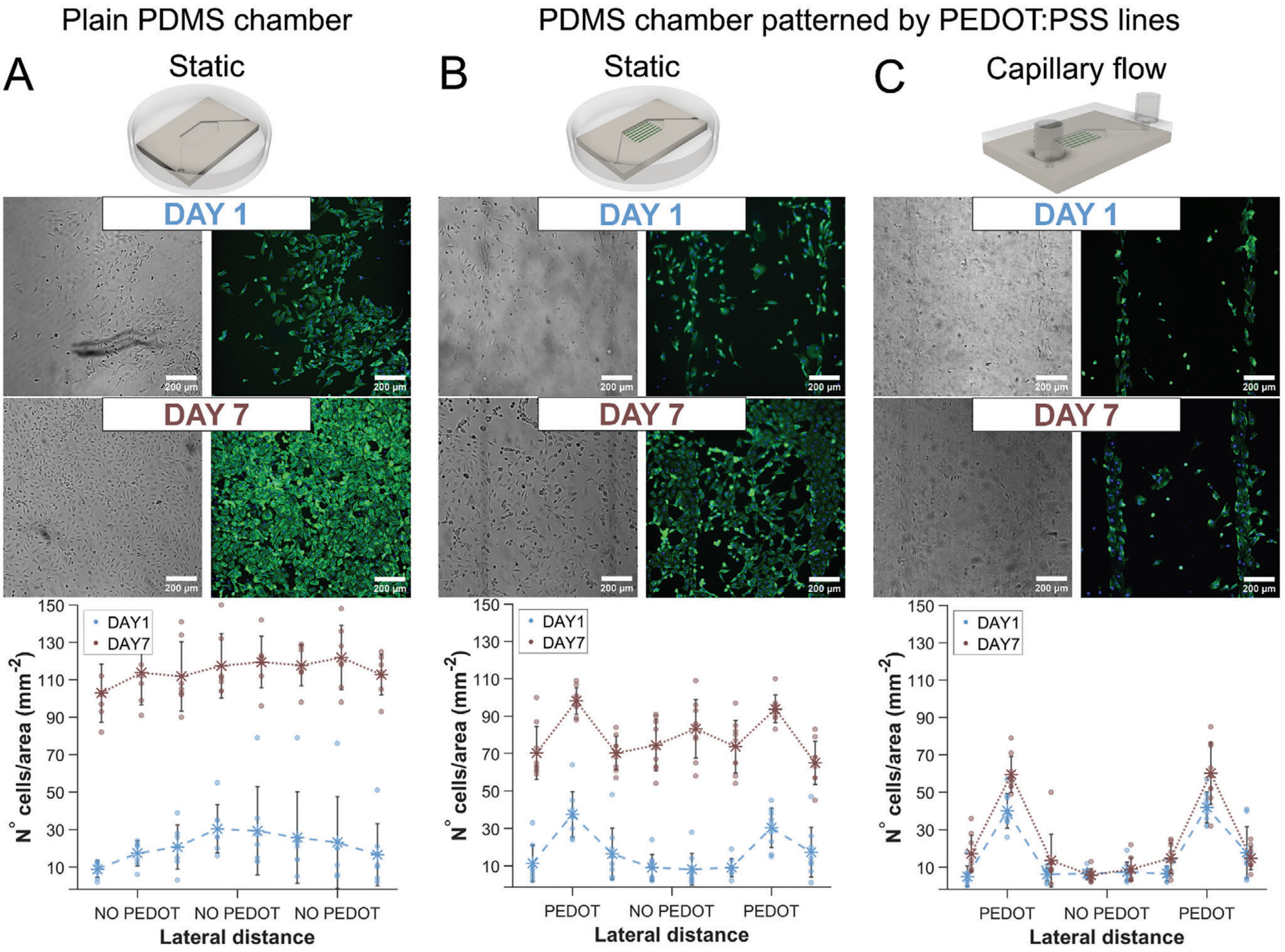

Figure 2. HUVEC culture and patterning efficiency in PEDOT:PSS-patterned PDMS device: A) on Matrigel-coated PDMS substrate, HUVECs show homogeneous distribution across the substrate; B,C) on patterned devices, HUVECs preferably adhere and proliferate along PEDOT:PSS; C) only under capillary flow HUVECs proliferate exclusively along the PEDOT:PSS lines. In the graphs (bottom row), asterisks denote the mean derived from 9 images (bars indicate standard deviation on $N = 9$ images across 3 devices) representing cell count per area (256 × 2048 pixels, 160 × 1280 μm^2, width × height). Each image was segmented into eight adjacent areas. For PEDOT:PSS-patterned devices (B,C), only two areas correspond with the PEDOT:PSS pattern and are labelled along the "Lateral distance" axis as "PEDOT," while the remaining areas lack the pattern and are labeled "NO PEDOT." (scale bars: 200 μm, fluorescent images: blue nuclei and green actin filaments).

device, facilitating endothelial cell adhesion. Figure 2C demonstrates pattern transparency preservation within the microfluidic device, enabling continuous optical monitoring of HUVECs culture progress. To assess the impact of oxygen plasma treatment on integrated PEDOT:PSS patterns, a comparative analysis of the untreated and plasma-treated lines was conducted examining topography, structural arrangement, and conductive properties. When using PEDOT:PSS tracks as a substrate for endothelial cell culture, the conductive behavior of the polymer can be exploited for real-time monitoring of the endothelial monolayer through Trans Endothelial Electrical (TEER) measurements. In this scenario, the tracks serve as transparent electrodes, precisely printed directly inside the microfluidic chamber by AJP, and must provide adequate conductivity behavior. A 30-second exposure to oxygen plasma (0.5 mBar, 13.56 MHz, 200 W), needed for microfluidic device assembly, effectively reduced PEDOT:PSS line thickness by 27.5% ($N = 9$ points across 3 lateral profiles) (**Figure** 3A,C). Based on Equation 2 (Experimental section), the thinner the pattern, the less the resistance to the passage of the liquid inside the chamber is affected. Moreover, the more homogeneous thickness post-exposure (Figure 3C) may favor a uniform cellular response. O_2 plasma-treated samples exhibited a significantly lower root mean square roughness (10.6 ± 3.6 nm, $N = 6$ AFM scans) compared to pristine samples (15.8 ± 2.7 nm) (Figure 3D). The roughness of standard commercially available substrates for cell culture generally falls below 10 nm,[56] bringing it closer to the values observed after treatment. Both untreated and exposed lines present nanograins on the surface (Figure 3A,B). Importantly, these features showed no statistically significant differences in height and lateral dimensions (height: 72.9 ± 21.2 nm, lateral dimension: 0.6 ± 0.2 μm for untreated samples; height: 65.3 ± 21.2 nm, lateral dimension: 0.7 ± 0.2 μm for O_2 plasma-treated, $N = 18$ grains across 3 AFM scans) and may have served as anchoring sites for endothelial cell adhesion.[57] Topographical analysis via AFM was complemented by the assessment of plasma treatment

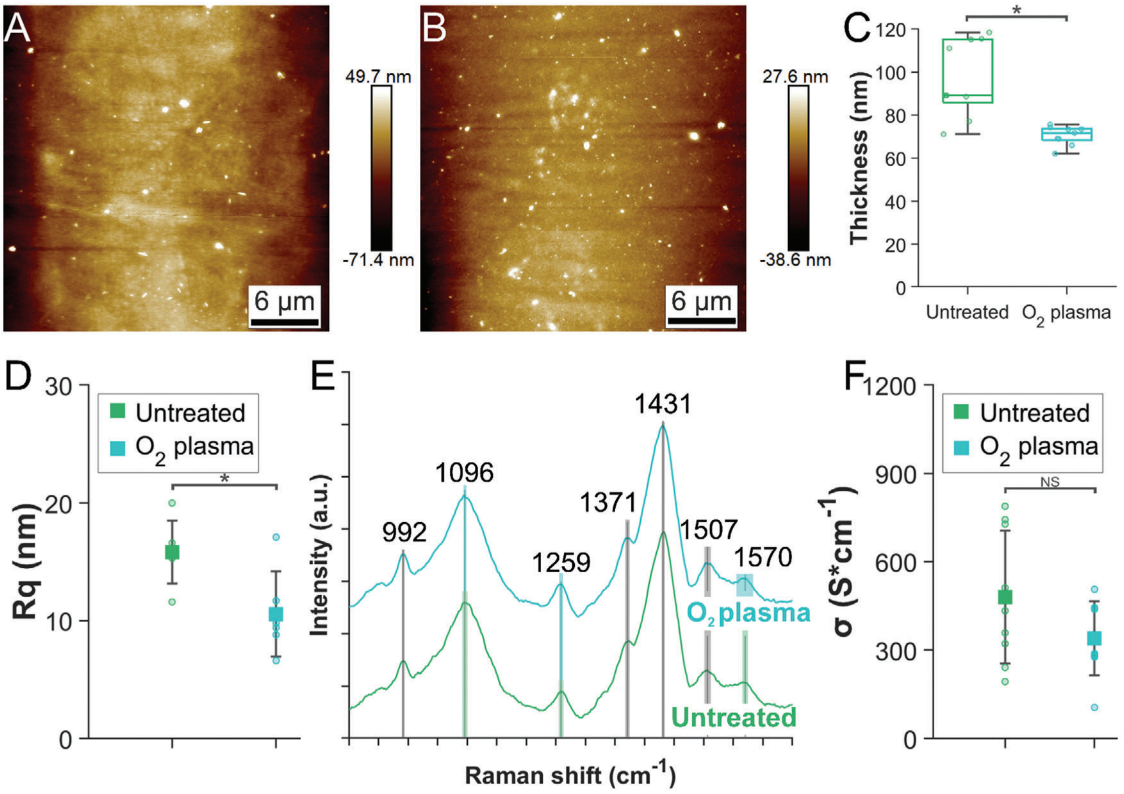

Figure 3. Effect of oxygen plasma treatment on PEDOT:PSS pattern. A) AFM scan of untreated PEDOT:PSS line (scale bar: 6 µm); B) AFM scan of O_2 plasma treated PEDOT:PSS line (scale bar: 6 µm); C) thickness of untreated (97.2 ± 18.0 nm) and O_2 plasma treated (70.5 ± 4.4 nm) PEDOT:PSS line ($N = 9$ points across 3 lateral profiles, $*p < 0.05$); D) root mean squared roughness of untreated (15.8 ± 2.7 nm) and O_2 plasma treated (10.6 ± 3.6 nm) PEDOT:PSS lines (bars indicate standard deviation on $N = 6$ AFM scans, $*p < 0.05$); E) average ($N = 9$) Raman spectra of untreated (bottom green line) and O_2 plasma treated PEDOT:PSS line aerosol jet printed onto glass substrate (shift from: 900 to 1650 cm^{-1}). Shadow areas indicating standard deviation on marked peak shift (grey shadow area: the standard deviations overlap between O_2 treated and untreated condition, blue and green shadow area: standard deviations are different between O_2 treated and untreated condition); F) electrical conductivity (σ) of untreated (480 ± 226 S cm^{-1}) and O_2 plasma treated (340 ± 126 S cm^{-1}) PEDOT:PSS lines (bars indicate standard deviation on $N = 9$ measurements, $*p < 0.05$, NS indicates no significance).

effects on the surface chemical composition and on the molecular structure of PEDOT:PSS respectively by XPS and Raman spectroscopy.

The XPS analysis showed evidence of plasma treatment oxidation of carbon and sulfur present at the surface of the PEDOT:PSS polymer blend. Comparison of element abundance before and after plasma treatment reveals a reduction in carbon content and an increase in oxygen and silicon content ($N = 3$ different PEDOT:PSS lines printed onto the same substrate, Table S1 in Supporting Information). The increase in oxygen is primarily attributed to oxidation caused by exposure to oxygen plasma, as confirmed by the presence of higher-energy species for both carbon (Table S2 in Supporting Information) and sulfur elements (Table S3 in Supporting Information). Detection of silicon originates from the glass substrate underneath the PEDOT:PSS pattern. Increasing in silicon content after plasma treatment can be attributed to the thickness reduction of the PEDOT:PSS patter (Figure 3A,B). Silicon speciation after plasma treatment of the substrate shows the presence of lower-energy species with a similar width of a peak at half maximum (FWHM), indicating localized oxidation that may be due to confined defects or thinning appearing in the PEDOT:PSS following plasma treatment. However, such defects are not visible by AFM topography (Figure 3B) and do not significantly affect the overall environment (Table S4 in Supporting Information).

The absence of significant changes in the peak shifts ($N =$ 9 spectra across 3 different PEDOT:PSS lines) in the Raman spectrum implies that the chemical bonds and molecular structures of PEDOT:PSS remain largely unaffected (Figure 3E). Thus, plasma etching of the surface does not induce degradation, decomposition, or substantial alterations in molecular arrangement.

PEDOT:PSS differs from other biocompatible polymers due to its unique electrical properties. The inherent conductivity is enhanced by the addition of ethylene glycol in the mixture. The precise deposition capability of AJP allows to print PEDOT:PSS tracks that can serve as electrodes or sensing components for example for in situ monitoring of cellular health. As a preliminary step to evaluate printed PEDOT:PSS electrical performance, its conductivity is assessed by 4-point measurement technique before and after O_2 plasma treatment. After exposure to oxygen plasma, printed PEDOT:PSS tracks exhibited a slight increase in electrical resistance, resulting in a marginal decrease in conductivity (σ = 480 ± 226 S cm^{-1} for untreated PEDOT:PSS and

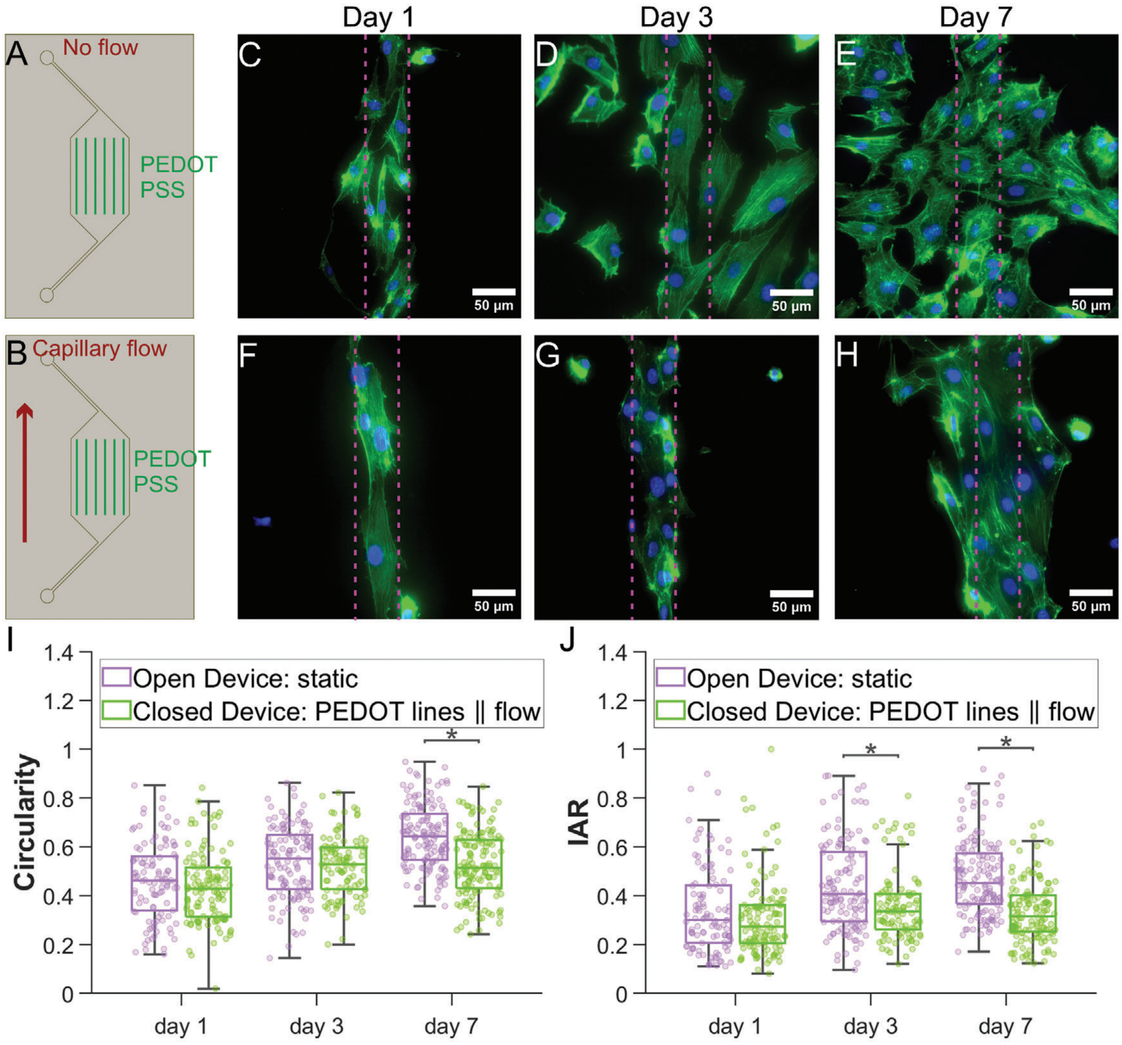

Figure 4. Elongation of HUVECs in PEDOT:PSS-patterned PDMS devices: A) schematic of a PEDOT:PSS-coated PDMS chamber; B) Schematic of a PEDOT:PSS-coated PDMS chamber subjected to capillary flow in the same direction (red arrow) as the patterned lines; C–E) HUVECs stained for F-actin (green) and nuclei (blue) on PEDOT:PSS lines under static conditions (dotted magenta lines highlight the position of the PEDOT pattern, scale bars: 50 μm); F–H) HUVECs stained for F-actin (green) and nuclei (blue) on PEDOT:PSS lines exposed to capillary flow in fully closed devices (dotted magenta lines highlight the position of the PEDOT pattern, scale bars: 50 μm); I) Circularity of HUVECs grown on the PEDOT:PSS lines within a PDMS chamber. For the open device, Circularity = 0.5 ± 0.2 at day 1 and day 3, Circularity = 0.7 ± 0.1 at day 7. For the closed device, Circularity = 0.4 ± 0.1 at day 1, Circularity = 0.5 ± 0.1 at day 3 and day 7; J) IAR of HUVECs grown on PEDOT:PSS lines within a PDMS chamber. For the open device, IAR = 0.3 ± 0.2, IAR = 0.4 ± 0.2, IAR = 0.5 ± 0.2 at day 7. For the closed device, constant IAR = 0.3 ± 0.2, at day 1, 3, and 7. In graphs (I,J): for open devices $N = 105$ at day 1, $N = 125$ at day 3, $N = 142$ at day 7 and for closed devices N = 121 at day 1, $N = 101$ at day 3, $N = 141$ at day 7 and for PEDOT:PSS lines perpendicular to flow $N = 131$ at day 1, $N = 139$ at day 3, and $N = 138$ at day 7, PEDOT:PSS is referred to as PEDOT, and $^*p < 0.05$.

$\sigma = 340 \pm 126$ S cm^{-1} for plasma-treated PEDOT:PSS, $N = 9$) (Figure 3F). This change is not statistically significant, indicating that it is unlikely to have a substantial impact on the electrical behavior of the material.

2.3. Combined PEDOT:PSS Patterning and Microfluidic Culture Enhances HUVECs Elongation and Alignment along Capillary Flow Direction

HUVECs cultured on the straight PEDOT:PSS pattern within the PDMS microchamber, initially adhere to the PEDOT:PSS surface, avoiding PDMS regions known to reduce cell adhesion.[58] Irrespective of flow conditions (schematics in **Figure** 4A,B), HUVECs exhibited a morphology mirroring the long and narrow PEDOT:PSS pattern up to 3 d post-seeding. Morphological analysis by means of shape descriptors reveals a non-circular morphology, elongated along the PEDOT:PSS lines (Figure 4C–H). Within the initial 72 h, circularity remains below 0.5 (Figure 4I) and Inverse aspect ratio (IAR) lower than 0.4 (Figure 4J) for HUVECs on PEDOT:PSS lines. Beyond the initial 3 d culture period, cell morphology varies based on distinct flow conditions and associated shear stress. In closed microfluidic chambers, cells experience cyclic shear stress every 12 h, from 6 dyn cm^{-2} gradually

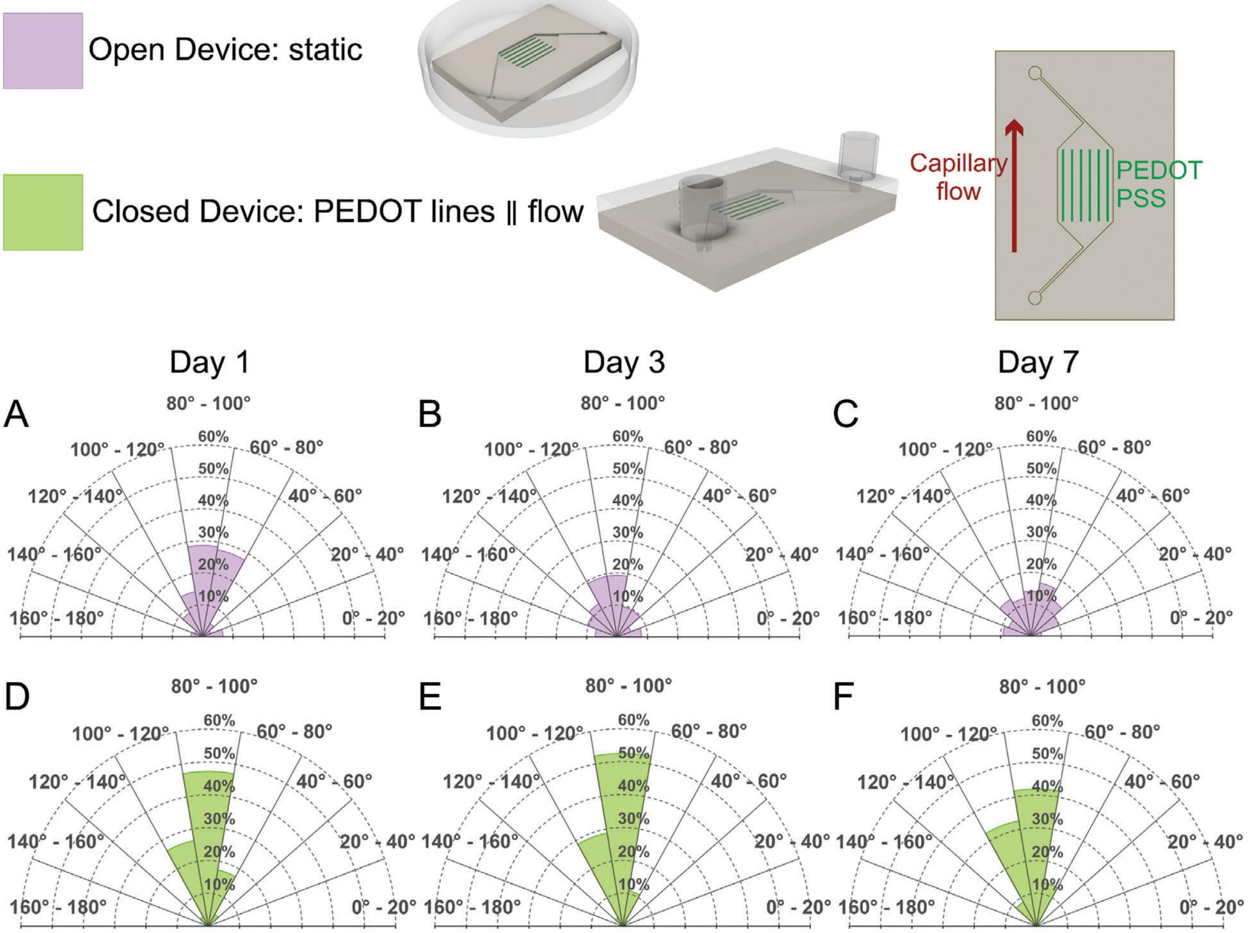

Figure 5. Alignment of HUVECs in a PEDOT:PSS patterned device: with reference to the legend and schematics of the 2 top rows where PEDOT:PSS lines are referred to as PEDOT lines; A–F) polar plots of cell alignment distribution where the 90° orientation indicates the direction of the PEDOT:PSS patterned lines. Evaluation is based on the major cell axis orientation. A) Polar plot for cells grown for one day ($N = 105$ cells), B) for 3 d ($N = 125$ cells) and C) for 7 d in static condition ($N = 142$ cells). D) Polar plot for cells grown for one day ($N = 121$ cells), E) for 3 d ($N = 101$ cells) and F) for 7 d under capillary flow ($N = 141$ cells).

diminishing to zero. The interplay of fluid flow and the enhanced adhesion provided by the PEDOT:PSS pattern, fostered cell elongation along the flow direction, consistent with the pattern orientation. After one week of culture, HUVECs growing in static conditions appeared more circular and less elongated (Figure 4D). They exhibit an average circularity greater than 0.5 (0.6 ± 0.1, $N = 142$ cells) and an IAR (0.5 ± 0.2, $N = 142$ cells). This is higher than that in capillary flow conditions, which remains lower and unchanged from the value evaluated on the third day of culture (0.3 ± 0.1 with $N = 101$ cells at day 3 and $N = 141$ cells at day 7) (Figure 4I).

The alignment along PEDOT:PSS line direction was facilitated by the interplay of capillary flow and pattern organization. Prior studies have demonstrated PEDOT:PSS-guided neural alignment on poly(potassium 3-sulfopropyl methacrylate) (PKSPMA) polymer brush coated glass substrate;[39] here we illustrate HUVEC cytoplasm alignment along the pattern direction on a PDMS surface. A comparison between static and capillary flow conditions reveals that cell alignment is accentuated and prolonged when HUVECs growing on PEDOT:PSS lines are subjected to shear stress in the same direction as the pattern. Within the first 24 h post-seeding, a higher percentage of cells subjected to capillary shear stress exhibits alignment along the PEDOT:PSS pattern. In static conditions (**Figure** 5A–C), approximately 29% of the analyzed cells ($N = 105$) showed long axis alignment with the pattern line direction (90° ± 10° for all panels in Figure 5) within 24 h post-seeding (Figure 5A). Under capillary flow (Figure 5D), this behavior was observed in nearly 50% (47%) of the cells ($N = 121$). The relative number of cells aligned with the pattern remained close to 50% during the first 3 days of culture (52% with $N = 101$ cells at the third day post seeding, Figure 5E) and decreased to 42% at the seventh day ($N = 141$ cells, Figure 5F). Overall, around 90% of the cells ($N = 121$ at day 1, $N = 101$ at day 3, $N = 141$ at day 7) aligned within the interval 90° ± 30° during the 7 d of culture under capillary flow (Figure 5D-F). This phenomenon was not observed in static conditions, where less than 20% of cells exhibits alignment along the pattern direction after 3 d of culture (19% with $N = 125$ cells at day 3 and 14% with $N = 142$ cells at day 7). Even when considering a wider interval of alignment (90° ± 30°), the cells with the major axis aligned do

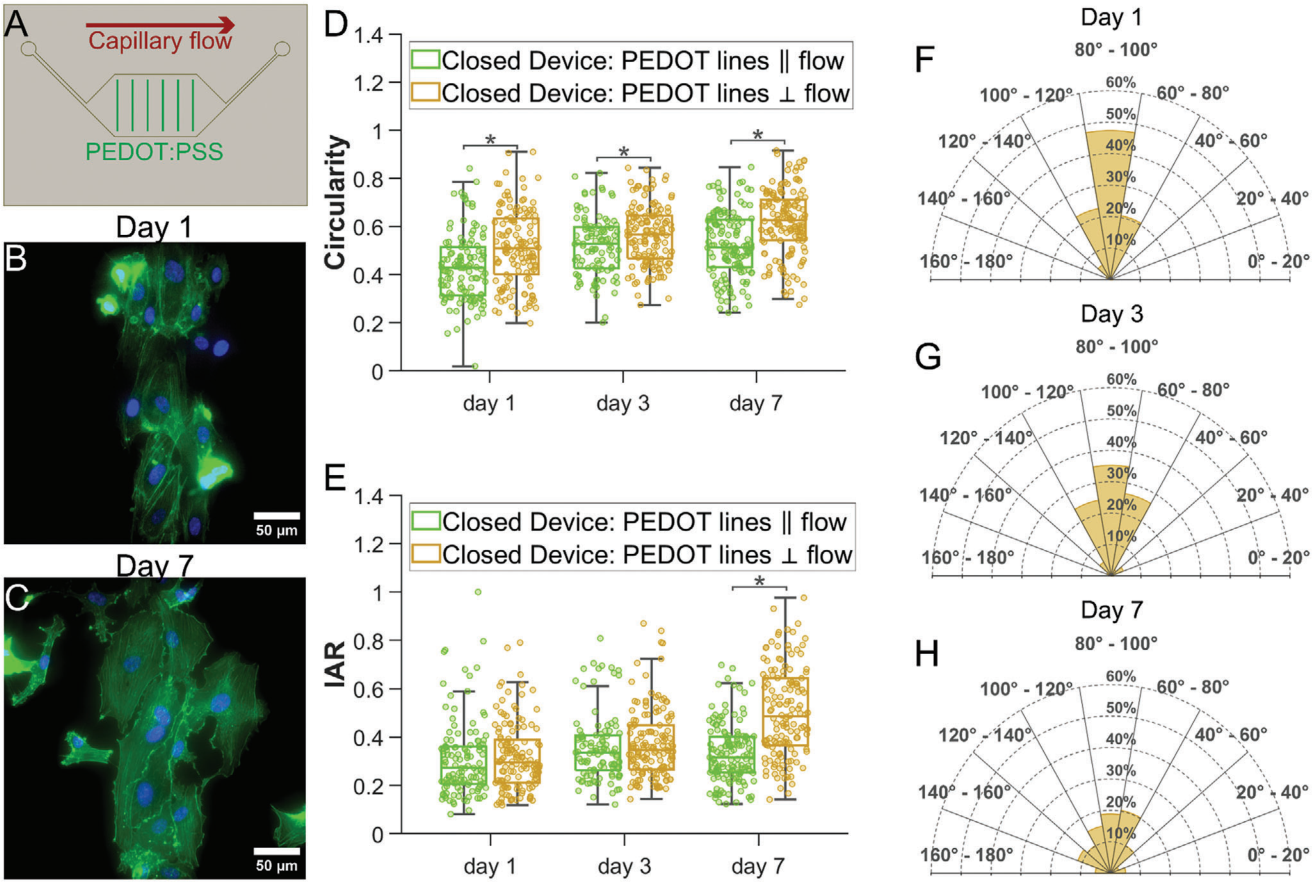

Figure 6. Elongation and alignment of HUVECs in a PDMS microfluidic device patterned by PEDOT:PSS lines perpendicular to the flow. A) Schematic of the flow direction (red arrow) relative to the PEDOT:PSS lines; B,C) HUVECs stained for F-actin and nuclei on the PEDOT:PSS lines under capillary flow (scale bars: 50 µm); D) Circularity of HUVECs on PEDOT:PSS lines under capillary flow. For lines parallel to the flow: Circularity = 0.4 ± 0.1 at day 1, Circularity = 0.5 ± 0.1 at day 3 and day 7. For lines perpendicular to the flow: Circularity = 0.5 ± 0.2 at day 1, Circularity = 0.6 ± 0.1 at day 3 and day 7 (PEDOT:PSS is referred to as PEDOT, $^*p < 0.05$); E) IAR of HUVECs on PEDOT:PSS lines under capillary flow. For lines parallel to the flow: IAR = 0.3 ± 0.2 at day 1,3,7. For lines perpendicular to the flow: IAR = 0.3 ± 0.1 at day 1, IAR = 0.4 ± 0.1 at day 3, and IAR = 0.4 ± 0. 2 at day 7 (PEDOT:PSS is referred to as PEDOT, $^*p < 0.05$); F–H) Polar plots of cell alignment distribution for PEDOT:PSS lines perpendicular to the flow. For all the graphs (D–H): for PEDOT:PSS lines parallel to flow $N = 121$ at day 1, $N = 101$ at day 3, $N = 141$ at day 7 and for PEDOT:PSS lines perpendicular to flow $N = 131$ at day 1, $N = 139$ at day 3, $N = 138$ at day 7.

not exceed 50% (48% with $N = 125$ cells at day 3 and 43% with $N = 142$ cells at day 7).

Under static conditions, stagnant larger volumes of endothelial cell medium may cause cells to spread beyond the pattern with nutrient deposition on the PDMS surface that creates a favorable environment for cell attachment. Higher medium volume may also accelerate HUVEC proliferation, leading to a loss of preference for the PEDOT:PSS pattern direction, resulting in a circular, less elongated morphology, and misalignment. To investigate whether this reduced volume alone enhances elongation and alignment or if this is the result of the combined effects of patterning and coherent capillary flow, we repeated the experiment, rotating the pattern lines by 90° to be perpendicular to the flow (**Figure** 6A). During all 7 days of culture, cells exhibit a more circular shape (Figure 6B,C) with a consistently significantly higher circularity value compared to those grown PEDOT:PSS lines parallel to flow (Figure 6D). At day 7 IAR reached 0.5 ± 0.2 denoting a further loss of elongation (Figure 6E). Cell elongation was indeed more pronounced when adhesive material patterns (PEDOT:PSS) and fluid flow synergistically stimulates cells along the same direction. A similar trend was observed in cellular alignment. Initially (at 24 hours post-seeding) (Figure 6F), the pattern direction appeared to be the predominant factor guiding cell alignment. Approximately 50% (47%) of the cells ($N = 131$ cells) aligned along the pattern direction (90° ± 10° in Figure 6F–H), with none aligned along the streamline (intervals 0°–20° and 160°–180° in Figure 6F–H). By day 3 (post-seeding), the percentage of cells aligned with the pattern decreased below 40% (35%, $N = 139$ cells) (Figure 6G). Finally, by day 7 of culture, the percentage of HUVECs aligned along the PEDOT:PSS lines further decreased to below 20% (18%, $N = 138$ cells) and 10% of cells aligned along the flow direction (Figure 6H).

3. Conclusions

Generating patterns of adhesive molecules inside microfluidic devices is a challenging task due to the lack of compatibility of bio-derived or adhesive materials with manufacturing steps, with chemicals and techniques for assembly, in particular with exposure to oxygen plasma. Utilizing AJP technology, we achieved high-resolution deposition of PEDOT:PSS inside a closed microfluidic chamber. The generated pattern enhanced adhesion of endothelial cells, favored rapid polarization and alignment in combination with capillary flow. The cellular adhesion and morphological changes on PEDOT:PSS patterns was previously demonstrated in terms of increased SH-SY5Y neurite and nuclei alignment on linear patterns with width ranging from 15 to 100 µm.[39,59] Similarly endothelial cells respond to patterned cytophilic lanes on cytophobic substrates, such as PDMS.[60] The adhesion is influenced by the patterned compound as well, and endothelial cells from different sources (arteries, veins, microvasculature) show different elongation and alignment on patterns of different widths. For vascular endothelial cells, such as HUVECs, the alignment is significantly affected by the micropatterned lane size. In particular, the alignment of HUVECs has been shown to increase when decreasing fibronectin strip width below 60 µm.[31]

In terms of height, in this study we focused on replicating the average thickness of protein coatings used for increasing adhesion of cells in vitro. In particular fibronectin alters the surface roughness forming typical features with thickness between 190 and 60 nm on PDMS, plain or plasma treated.[61] The adhesion and spreading of singles cells on the 100 nm high pattern resulted significantly higher than on untreated PDMS (see Figure S4, Supporting Information).

PEDOT:PSS is also conductive, transparent, remains conductive after device assembly and thus it is useful for designing sensors and electrodes inside a microfluidic device or organ-on-a-chip systems. While further assessment of the conductivity of the pattern once in contact with liquid/cells is needed, there are numerous applications of PEDOT:PSS for detecting cellular activity, where the conductivity is confirmed either in wet and dry conditions.[62] Having demonstrated the compatibility of the aerojet jet printing of the conductive polymer with soft lithographic techniques for assembly microfluidic devices, the technique can now be adopted for the design of electrodes for effective assessment of trans-epithelial electric resistance, of sensors for in situ metabolite recognition adopting approaches previously used for development for recording and modulation of electrophysiological and biochemical cell signals in for bioelectronic devices.[62]

Patterning PEDOT:PSS strengthened the alignment of the cells: interestingly, under static conditions the cell pattern, elongation and alignment are lost after 3 d, confirming the importance of capillary flow. The loss of cellular alignment was observed between the third and seventh day of culture when the pattern orientation was opposite to the direction of capillary flow. This confirmed the concurrence of both stimuli, fluidic and topographical in maintaining cellular alignment.

This microfluidic device, integrating PEDOT:PSS pattern, not only facilitates controlled EC alignment without the need for external active pumps, but also capitalizes on the unique properties of a conductive polymer pattern, endowing the system with the potential to serve as an electrical sensor.

4. Experimental Section

PDMS Layer Preparation: PDMS rhomboidal chamber (width: 6.2 mm, length: 8 mm, depth: 100 µm, schematic and dimensions in Figure S5 in Supporting Information) were fabricated by cast and curing (overnight at 65 °C) liquid PDMS (polymer:curing agent, 10:1) on SU8 2075 molds. To obtain the desired 100 µm thickness, SU8 2075 negative photoresist (Kayaku Advanced Materials, MA, USA) was spin coated on a cleaned silicon wafer at 200 rpm for 10s, 400 rpm for 10s, 600 rpm for 10s then at 1900 rpm for 40s. Samples were then baked for 120 min at 55 °C. Mold exposure was then performed with MicroWriter ML direct-write laser photography machine (Durham Magneto Optics Ltd, UK) using an energy dose of 200 mJ cm^{-2}. Post-exposure baking was done at 55 °C for 120 min. Resist development was obtained in EC-solvent for 10 min followed by 1 min rinse in fresh solvent.

PEDOT:PSS Deposition by AJP: A solution containing PEDOT:PSS (Clevios PH 1000, Heraeus Epurio) was diluted with ethylene glycol (20% v/v, >99.8%, Sigma Aldrich) and 3-glycidyloxypropyl)trimethoxysilane (GOPS) (0.2% v/v, >98%, Sigma Aldrich) and used as the print material.[40,39] The suspension was ultrasonically agitated for 10 minutes prior to printing to break up agglomerates and disperse the particles. 1.5 mL of the prepared PEDOT:PSS formulation was processed in the ultrasonic atomizer of the aerosol jet printer (Optomec Aerosol Jet print engine, Optomec Inc.). A schematic of the AJP apparatus and process used in this work is illustrated in Figure S6 in Supporting Information. From previous studies, the print parameters were set to print lines with a maximum height in the order of a few hundred of nanometers and a width of 50 µm.[39] A 200 µm nozzle, sheath gas flow rate of 60 SCCM, carrier gas flow rate of 25 SCCM, stage speed of 2 mm s^{-1} and Z height above the substrate surface of 2.5 mm were used throughout. Gas flow rates are quoted in standard cubic centimeters per minute (SCCM). PDMS rhomboidal chambers and standard microscope slides (Thermo Fisher Scientific, USA) were used as printing substrates. Immediately prior to printing, the PDMS chambers were treated for 1 min with oxygen plasma to create a hydrophilic surface and facilitate the spreading of the PEDOT:PSS water dispersion and the printing of homogeneous patterns. The pattern printed on the bottom of the PDMS chamber consisted of six parallel straight lines of 50 µm width with 180 µm pitch (Figure S7 in Supporting Information). Regarding the printing on glass slides (used for Raman spectroscopy, four-point measurements and X-ray photoelectron spectroscopy (XPS)), wider patterns were obtained by printing multiple connected parallel lines with a small shift of around 50 µm in between each line, to gradually build the width up to the millimeter scale. The ink showed good wetting on glass slides and hence no surface pre-treatment was required. After printing, the substrates were placed in an oven at 100 °C for 10 min to drive off solvents and make the PEDOT:PSS resistant to water.

AFM Imaging and Scan Analysis: AFM images were acquired with Bruker Dimension Fastscan (Santa Barbara, CA, USA) equipped with either the Dimension Fastscan scan head (for images under 30 × 30 µm) or the Dimension Icon scan head (for images under 100 × 100 µm). For the dimension icon scan head, the samples were imaged with the PFQNM-LC-A-CAL cantilevers (Bruker) using peakforce tapping mode in air, at a scan rate of 0.1 Hz, with amplitude setpoint at 250 mV and driven at 1130 mV. The image was acquired with a pixel resolution of 256 × 256. For the Fastscan scan head, the SCOUT 350 HAR cantilever was used (NuNano), the peakforce tapping mode was used in air with a scan rate of 3 Hz, amplitude was set at 300 mV and the cantilever was driven at 17 mV, images were acquired with a pixel resolution of 1024 × 1024. Images acquisition was carried out via the ScanAsyst imaging mode via the Nanoscope software and analyzed were carried out with Nanoscope analysis 1.9. The thickness before and after plasma exposure is assessed by acquiring two scans along the same line of the pattern, before and after the treatment. These scans are conducted along the edge of the line. For each scan, three surface profiles are traced across the edge of the line, and three thickness values are extracted from each traced profile ($N = 9$ points across 3 height profiles). For roughness analysis before and after treatment, 18 scans were taken ($N = 9$, 9 scans before and 9 scans after treatment). 18 nanograins across 3 scans before treatment and 18 nanograins across 3 scans after treatment were selected and relative surface profile analyzed to extract width and height of the features.

Device Assembly: Two types of devices were assembled; closed microfluidic devices and open devices. Closed devices are composed by two PDMS layers: the lower layer is a PDMS chamber patterned with PEDOT:PSS line deposited by AJP, and the upper layer is a 5mm-thick plain PDMS block where inlet and outlet ports are opened by punching holes of 1.5 mm (Integra Miltex, NJ, USA). To seal the devices, both bottom and top layers are exposed to Oxygen plasma (0.5 mBar, 13.56 MHz, 200 W, 30 s, Diener electronic GmbH & Co. KG, Germany) and pressed together. Pyrex cloning cylinders (Fisher Scientific, PA, USA), attached with liquid PDMS, serve as reservoirs for cell medium at the inlet and outlet, providing a total volume of 500 µL each. Open devices are PDMS chambers coated with PEDOT:PSS line deposited by AJP, lying inside a tissue culture treated Petri dish (Ø 35 mm, CytoOne, Belgium). Figure S7 in Supporting Information illustrates a schematic representation of the different device assemblies. For consistency with the closed devices, the layers intended for use in open devices were also treated with oxygen plasma, even though strictly necessary.

Cell Culture and Device Seeding: The study was performed with commercially available cells, not acquired from tissues during the project. The project was carried out according to the Ethical Guidelines of the 1975 Declaration of Helsinki and following revisions. In particular, human umbilical vein endothelial cells (HUVECs, Lonza, Switzerland) were cultured in conventional T75 flask up to passage 10 and maintained at 37 °C and 5%CO_2. Endothelial cell medium was supplemented with 1% endothelial cell growth supplement (ECGS), 5% fetal bovine serum (FBS), 1% Pen-Strep mixture (ScienCell, CA, USA). Prior to cell seeding the devices where covered, if opened, or filled, if closed, first by ethanol cleaning solution (70% in deionized water), washed three times with phosphate-buffered saline (PBS) end then once with complete medium. For device seeding, 1×10^6 cells were suspended into 1 mL of complete ECM and either plated directly on top of the patterned PDMS layer in open devices or loaded inside the fully closed patterned microfluidic devices (≈100 µL each device). In open devices, right after seeding, PDMS layers were covered with 1 mL of complete medium that was refreshed every 24 h. In closed devices, cells were allowed to attach for 30 minutes, and medium was replaced by emptying and refilling the inlet reservoir with 500 µL of fresh complete medium twice a day. Cells were maintained in the devices for up to 7 days. Pattern-free control devices were coated with a thin layer of Matrigel (Corning Inc., USA) diluted in fresh medium (Matrigel:medium, 1:50). PDMS chambers were left under Matrigel coating for 3 h, followed by three washes in PBS and one in complete endothelial cell medium before seeding.

Cell Maintenance in the Devices and Capillary Flow: In fully enclosed microfluidic chambers, HUVECs were subjected to capillary flow, driven by the liquid cell medium's natural tendency to reach equilibrium between the inlet and outlet reservoirs. The flow rate (Q) was approximated using the Hagen-Poiseuille equation

$$Q = \frac{\Delta P}{R_H} \tag{1}$$

where ΔP is the difference in hydrostatic pressure between the inlet and outlet ($\Delta P = \rho g \Delta H$). ρ is the density of the liquid medium (considered as water) at 37 °C, ΔH is the liquid height difference between the inlet and outlet reservoirs, and R_H denotes the hydrodynamic resistance of the microfluidic chamber. R_H can be estimated as[63]

$$R_H = \frac{12\eta l}{\left(1 - 0.63\frac{h}{w}\right)} \frac{1}{h^3 w} \tag{2}$$

The assessment of shear stress follows a simplified formula for microfluidic perfusion culture in 2D Poiseuille flow systems:

$$\tau = 6\frac{\eta Q}{w h^2} \tag{3}$$

For both R_H and τ, η is the dynamic viscosity of water, l is the length of the micrometric chamber (Figure S5 in Supporting Information), w its width (Figure S5 in Supporting Information), and h its height (100 µm). Cells experience peak shear stress every 12 h when the inlet reservoir is replenished with medium, and ΔH matches the total height of the reservoir (1 cm). This calculation assumes fully developed flows in a chamber where w exceeds h.

Flow Resistance Test and Simulation: The assessment of cell adhesion to the PEDOT:PSS pattern under fluidic shear stress involved conducting a flow test at room temperature. After a 7 d culture of HUVECs, three closed devices patterned with PEDOT:PSS lines parallel to the flow direction were connected to a syringe pump (KF Technology, Italy) using Tygon tubing (internal diameter: 0.020″ and outer diameter: 0.060″) (Cole Parmer, USA) and 24G blunt needle connections (Sai Infusion Technologies, USA). Fresh cell medium was used for the flow test, and the spent medium was collected through tubing connected to the outlet port. Before the test, cells were stained with Neutral Red (Sigma-Aldrich, USA, 30 µL of Neutral Red in 2 mL of fresh ECM) for visualization under an inverted phase-contrast microscope (VWR, VisiScope IT404, Profcontrol GmbH, Germany) equipped with a camera (GXCAM HiChrome HR4 Lite, GT Vision, UK). The average shear stress experienced by the cells was calculated using the formula in Equation 1. The flow was incrementally increased in 50 $\mu L\ min^{-1}$ steps from 100 to 500 $\mu L\ min^{-1}$, with cells exposed to each flow rate for 30 min. Following the experiment, cells were allowed to recover for 2 h in the incubator at 37 °C and 5%CO_2. Images of cells were captured before the flow test and after the recovery time following the experiment, with six pictures for each device taken across different patterning lines in both instances.

To observe the velocity distribution in the chamber at the highest flow rate (500 $\mu L\ min^{-1}$), a fine mesh 3D COMSOL simulation (COMSOL Multiphysics v.6.1) was performed. Water was modeled as a Newtonian, incompressible, and homogeneous fluid flowing within the device. The simulation assumed a no-slip condition at the walls, zero pressure at the outlet, laminar flow, and negligible effects of chamber wall deformations. The microfluidic chamber design was imported as a. dwg file generated by Fusion 360 software and then extruded to obtain the chamber height (100 µm). The COMSOL Computational Fluid Dynamics (CFD) package solves the Navier-Stokes equations for mass and momentum conservation (Figure S8, Supporting Information).

Fluorescence Staining and Imaging: To perform viability, patterning efficiency, alignment, and elongation study, HUVECs were stained with NucBlue Live reagent (Hoechst 33342) and Propidium iodide (ReadyProbes Cell Viability Imaging Kit (Blue/Red), Molecular Probes, USA) to label nuclei and with phalloidin (ActinGreen 488 Ready Probes, ThermoFisher Scientific, UK) to label acting filaments (F-Actin). F-Actin staining was performed after washing cell three times in PBS, fixing with 4% paraformaldehyde for 10 min at room temperature, and rinsing with PBS. Bright field and fluorescent images of cells were acquired with an inverted microscope system (Nikon ECLIPSE Ti2, Nikon Instruments Inc., NY, USA) equipped with a Digital CMOS camera (ORCA Flash4.0 V3, Hamamatsu Photonics, Japan) and a LED illumination system (pE-4000 CoolLED, MA, USA).

Raman Spectroscopy: Raman spectroscopy was performed on ≈50 µm wide and ≈100 µm thick PEDOT:PSS line deposited by AJP on standard microscope slides (Thermo Fisher Scientific, USA). Raman spectra were collected using a Horiba LabRAM HR Evolution microscope using a 50 W 532 nm (green) laser passing through an ultra low frequency (ULF) filter at 50 × magnification. A hole size of 50 µm and laser powers of 5% was used, and the grating was 600 grooves per mm, and 20 s per scan and the data were averaged over 2 passes using LabSpec 6 software. Using MATLAB programming language (The Mathworks, MA, USA) spectra were initially segmented to isolate the signal of interest (shift from 900 to 1650 cm^{-1}), in accordance with the literature.[64] Once segmented, each individual spectrum underwent baseline correction, and high-frequency noise was mitigated through rolling-average denoising. For each spectrum ($N = 9$ spectra for treated and untreated samples across three different PEDOT:PSS lines), 7 major peak shifts were manually identified and compare between O_2 plasma treated and untreated samples.

X-Ray Photoelectron Spectroscopy (XPS): The glass samples (with printed PEDOT:PSS lines on) were mounted onto the sample plate and the printed lines were earthed using carbon tape, to the plate. XPS spectra were collected using a Thermo Escalab 250 XPS instrument equipped with a monochromatic Al Kα X-ray source (150 W). Survey scans were collected between 0 and 1250 eV with a pass energy of 150 eV. The spot size was 500 µm and the analyses were done with a power of 150 W. High-resolution spectra were collected with a pass energy of 20 eV and a step size of 0.1 eV. The data was processed, and binding energies corrected with the CasaXPS software using the C1s (C–C species) peak at 285 eV with relative sensitivity factors for the individual elements based upon the scheme where $C = 1$.

Four-Point Measurements: Four-point measurements were performed on ≈3 mm wide, ≈100 µm thick and 3 cm long PEDOT:PSS lines deposited by AJP on standard microscope slides (Thermo Fisher Scientific, USA). Measurements were performed across 3 lines ($N = 9$ measurements across 3 PEDOT:PSS lines). IV curves were collected using a Keithley Sourcemeter (2400 series) which was configured in four-probe mode. Acquisition was performed using in-house custom Python script. The sample was positioned on a polytetrafluoroethylene (PTFE) stage beneath four measurement round-tip, 1.5 mm-spaced probes (Coda Systems, UK) held in place by an additional PTFE block. The probes were fastened or released using lateral screws and were connected to input current and output voltage pins accordingly to the source meter manual instructions.

The linear portion of the IV curves was isolated using MATLAB programming language (The Mathworks, MA, USA). The resistance of the PEDOT:PSS lines was then evaluated using the formula:

$$R = C\frac{\Delta V}{\Delta I}$$

where $\frac{\Delta V}{\Delta I}$ is the gradient of the linear portion of the I–V curve and C is a correction factor that accounts for the finite width of the PEDOT:PSS line.[65] Subsequently, resistivity was calculated from the obtained resistance, and conductivity (σ) was derived.

Image and Data Analysis: Cell counting from bright field images was manually performed using ImageJ software, both before and after the flow resistance test ($N = 18$ images across 3 devices). For fluorescence images of the nuclei, MATLAB programming language (The Mathworks, MA, USA) was employed. The process involved initial binarization of the images, followed by morphological opening. Subsequently, watershed transformation was applied, and foreground pixels connected with a connectivity of 8 pixels were counted as cell nuclei ($N = 9$ images across 3 devices for each condition of flow). For the patterned devices, images were uniformly rotated to ensure vertical alignment of the PEDOT:PSS lines. Subsequently, the images were partitioned into eight adjacent areas, each measuring 256 × 2048 pixels (160 × 1280 µm^2 in width × height). The regions designated as "PEDOT" areas, corresponding to PEDOT:PSS lines, were identified as the 2nd and 7th areas when counting from left to right. All other areas were categorized as "NO PEDOT" regions. A visual representation of this image segmentation is provided in Figure S9 in the Supporting Information. Cell morphology was quantified using shape descriptors. Initially, images were aligned vertically, considering the direction of the pattern lines as 90°. Subsequently, cell boundaries were manually outlined using the freehand line tool in ImageJ. ($N = 105$, 121, 131 cells outlined at day 1, $N = 125$, 101, 139 at day 3 and $N = 142$, 141, 138 at day 7 respectively for static conditions, capillary flow pattern lines aligned with the flow and capillary flow with pattern lines perpendicular to the flow direction). Cell elongation was assessed through shape descriptors, specifically circularity and axis lengths. Circularity (C) is computed using the formula $C = \frac{4\pi A}{2P}$ where A is the area and $2P$ the perimeter of the projected cell. A circularity value of 1.0 indicates a perfect circle, while a value close to 0.0 suggests an elongated cell shape. Inverse aspect ratio (IAR) is derived from axis lengths, calculated as the length of the short axis divided by the length of the long axis. Cell orientation is evaluated by determining the orientation angle of the cell's long axis with respect to the horizontal axis of the image, which is perpendicular to the PEDOT:PSS pattern lines. This angle is quantified as Feret's angle (θ) by ImageJ software. Polar plots illustrate the percentage of cells aligned within specific direction ranges, with the 80°–100° range considered the one aligning best with the pattern. The direction ranges include 0°–20°, 20°–40°, 40°–60°, 60°–80°, 80°–100°, 100°–120°, 120°–140°, 140°–160°, and 160°–180°. Data were plotted and analyzed by one-way analysis of variance (ANOVA), using MATLAB programming language (The Mathworks, MA, USA). Statistical significance was determined when p-value < 0.05. In the text data are always reported as mean ± standard deviation.

Supporting Information

Supporting Information is available from the Wiley Online Library or from the author.

Acknowledgements

This work was funded by the European Union's Horizon 2020 research and innovation 7 program under the Marie Skłodowska-Curie MSCA-ITN grant agreement no. 812398, through the single-entity nanoelectrochemistry, SENTINEL project. S.T. and R.H. acknowledge funds from Engineering and Physical Sciences Research Council (EPSRC) under grants EP/P027687/1 and EP/V009818/1. C.C.C.C. acknowledges funds from the Engineering and Physical Sciences Research Council UK (EPSRC) Healthcare Technologies for the grant EP/W004933/1.

Conflict of Interest

The authors declare no conflict of interest.

Author Contributions

E.M. designed all the experiments, manufactured the devices, and performed all the experiments. S.T. and R.H. optimized the AJP methods and prepared the substrates for the characterization measurements and for the microfluidic culture. E.S., C.C.C.C, N.J., B.J. supported E.M., respectively, for the characterization with Raman Spectroscopy and COMSOL modeling, AFM, 4-point measurement and XPS. R.H. and K.C. defined the best practice for the AJP and for the characterization methods. V.P. led the conceptualization, identification of methodology, supervision and review and complete review and editing. All the authors contributed to the writing of the original draft and editing of figures and Supporting Information. The authors thank Prof. Stephen Evans for his contribution to the development and the use of the 4 probe set up for conductive measurements.

Data Availability Statement

The data that support the findings of this study are openly available in Research Data Leeds Repository at https://doi.org/10.5518/1503, reference number 1503.

Keywords

aerosol jet printing, cell adhesion, microfluidics PEDOT:PSS

Received: March 11, 2024
Revised: May 15, 2024

[1] Y. Chen, L. Ju, M. Rushdi, C. Ge, C. Zhu, *Mol. Biol. Cell* **2017**, *28*, 3134.
[2] Y. Zhang, P. Habibovic, Y. Zhang, P. Habibovic, *Adv. Mater.* **2022**, *34*, 2110267.
[3] Y. Li, G. Huang, X. Zhang, L. Wang, Y. Du, T. J. Lu, F. Xu, *Biotechnol. Adv.* **2014**, *32*, 347.
[4] F. Yang, Y. Zhang, J. Zhu, J. Wang, Z. Jiang, C. Zhao, Q. Yang, Y. Huang, W. Yao, W. Pang, L. Han, J. Zhou, *Front. Bioeng. Biotechnol.* **2020**, *8*, https://doi.org/10.3389/fbioe.2020.00647.
[5] P. F. Davies, C. Shi, N. DePaola, B. P. Helmke, D. C. Polacek, *Ann. N. Y. Acad. Sci.* **2001**, *947*, 7.
[6] R. Steward, D. Tambe, C. Corey Hardin, R. Krishnan, J. J. Fredberg, *Am. J. Physiol.: Cell Physiol.* **2015**, *308*, C657.
[7] S. Fleischer, D. Naveed Tavakol, G. Vunjak-Novakovic, S. Fleischer, D. N. Tavakol, G. Vunjak-Novakovic, *Adv. Funct. Mater.* **2020**, *30*, 1910811.
[8] S. E. Shelton, *Curr. Opin. Hematol.* **2024**, *31*, 155.
[9] E. Roux, P. Bougaran, P. Dufourcq, T. Couffinhal, *Front. Physiol.* **2020**, *11*, 533349.
[10] Q. Zhong, H. Ding, B. Gao, Z. He, Z. Gu, *Adv. Mater. Technol.* **2019**, *4*, 1800663.
[11] U. M. Sonmez, Y. W. Cheng, S. C. Watkins, B. L. Roman, L. A. Davidson, *Lab Chip* **2020**, *20*, 4373.
[12] V. S. Shirure, S. Yechikov, B. S. Shergill, T. Dehghani, A. V. Block, H. Sodhi, A. Panitch, S. C. George, *Lab Chip* **2023**, *23*, 3050.
[13] I. Pediaditakis, K. R. Kodella, D. V. Manatakis, C. Y. Le, C. D. Hinojosa, W. Tien-Street, E. S. Manolakos, K. Vekrellis, G. A. Hamilton, L. Ewart, L. L. Rubin, K. Karalis, *Nat. Commun.* **2021**, *12*, 5907.
[14] R. Pajoumshariati, L. Ewart, V. Kujala, R. Luc, S. Peel, A. Corrigan, H. Weber, B. Nugraha, P. B. L. Hansen, J. Williams, *Adv. Sci.* **2023**, *10*, 2303131.
[15] S. Kim, J. Park, J. N. Ho, D. Kim, S. Lee, J. S. Jeon, *Biofabrication* **2023**, *15*, 045016.
[16] K. Rennert, S. Steinborn, M. Gröger, B. Ungerböck, A. M. Jank, J. Ehgartner, S. Nietzsche, J. Dinger, M. Kiehntopf, H. Funke, F. T. Peters, A. Lupp, C. Gärtner, T. Mayr, M. Bauer, O. Huber, A. S. Mosig, *Biomaterials* **2015**, *71*, 119.
[17] X. Wang, B. Xu, M. Xiang, X. Yang, Y. Liu, X. Liu, Y. Shen, *Microvasc. Res.* **2020**, *128*, 103930.
[18] N. Baeyens, S. Nicoli, B. G. Coon, T. D. Ross, K. Van Den Dries, J. Han, H. M. Lauridsen, C. O. Mejean, A. Eichmann, J. L. Thomas, J. D. Humphrey, M. A. Schwartz, *eLife* **2015**, *2015*, 4.
[19] A. L. Paguirigan, D. J. Beebe, *Integr. Biol.* **2009**, *1*, 182.
[20] H. Yu, C. M. Alexander, D. J. Beebe, *Lab Chip* **2007**, *7*, 726.
[21] S. Giulitti, E. Magrofuoco, L. Prevedello, N. Elvassore, *Lab Chip* **2013**, *13*, 4430.
[22] S. Halldorsson, E. Lucumi, R. Gómez-Sjöberg, R. M. T. Fleming, *Biosens. Bioelectron.* **2015**, *63*, 218.
[23] J. Wang, H. Wang, X. Mo, H. Wang, *Adv. Mater.* **2020**, *32*, 2004555.
[24] C. W. Hsiao, M. Y. Bai, Y. Chang, M. F. Chung, T. Y. Lee, C. T. Wu, B. Maiti, Z. X. Liao, R. K. Li, H. W. Sung, *Biomaterials* **2013**, *34*, 1063.
[25] C. A. Dessalles, C. Leclech, A. Castagnino, A. I. Barakat, *Commun. Biol.* **2021**, *4*, 1.
[26] S. J. Liliensiek, J. A. Wood, J. Yong, R. Auerbach, P. F. Nealey, C. J. Murphy, *Biomaterials* **2010**, *31*, 5418.
[27] S. Pradhan, O. A. Banda, C. J. Farino, J. L. Sperduto, K. A. Keller, R. Taitano, J. H. Slater, *Adv. Healthcare Mater.* **2020**, *9*, 1901255.
[28] W. Liu, Q. Sun, Z. L. Zheng, Y. T. Gao, G. Y. Zhu, Q. Wei, J. Z. Xu, Z. M. Li, C. S. Zhao, *Small* **2022**, *18*, 2104328.
[29] J. Yoo, T. H. Kim, S. Park, K. Char, S. H. Kim, J. J. Chung, Y. Jung, *Adv. Funct. Mater.* **2021**, *31*, 2008172.
[30] S. W. Rhee, A. M. Taylor, C. H. Tu, D. H. Cribbs, C. W. Cotman, N. L. Jeon, *Lab Chip* **2005**, *5*, 102.
[31] C. C. Wu, Y. S. Li, J. H. Haga, R. Kaunas, J. J. Chiu, F. C. Su, S. Usami, S. Chien, *Proc. Natl. Acad. Sci. USA* **2007**, *104*, 1254.
[32] M. Théry, M. Piel, *Cold Spring Harbor Protoc.* **2009**, *4*, pdbprot5255.
[33] P. Shi, S. Nedelec, H. Wichterle, L. C. Kam, *Lab Chip* **2010**, *10*, 1005.
[34] C. Tu, B. Huang, J. Zhou, Y. Liang, J. Tian, L. Ji, X. Liang, X. Ye, *Micromachines* **2017**, *8*, 1.
[35] E. B. Secor, *Flexible Printed Electron.* **2018**, *3*, 035002.
[36] N. J. Wilkinson, M. A. A. Smith, R. W. Kay, R. A. Harris, *Int. J. Adv. Manuf. Technol.* **2019**, *105*, 4599.
[37] M. N. De Silva, J. Paulsen, M. J. Renn, D. J. Odde, *Biotechnol. Bioeng.* **2006**, *93*, 919.
[38] E. W. C. Phuah, W. L. Hart, H. Sumer, P. R. Stoddart, *Bioprinting* **2020**, *18*, e00081.
[39] A. J. Capel, M. A. A. Smith, S. Taccola, M. Pardo-Figuerez, R. P. Rimington, M. P. Lewis, S. D. R. Christie, R. W. Kay, R. A. Harris, *Front. Cell Dev. Biol.* **2021**, *9*, https://www.frontiersin.org/articles/10.3389/fcell.2021.722294.
[40] M. Mirbagheri, V. Adibnia, B. R. Hughes, S. D. Waldman, X. Banquy, D. K. Hwang, *Mater. Horiz.* **2019**, *6*, 45.
[41] K. Zhang, X. Xiao, X. Wang, Y. Fan, X. Li, *J. Mater. Chem. B* **2019**, *7*, 7090.
[42] Y. Shi, K. Liu, Z. Zhang, X. Tao, H.-Y. Chen, P. Kingshott, P. Y. Wang, *ACS Biomater. Sci. Eng.* **2020**, *6*, 1836.
[43] J. M. Karp, Y. Yeo, W. Geng, C. Cannizarro, K. Yan, D. S. Kohane, G. Vunjak-Novakovic, R. S. Langer, M. Radisic, *Biomaterials* **2006**, *27*, 4755.
[44] R. Kane, *Biomaterials* **1999**, *20*, 2363.
[45] M. Ermis, A. Ezgi, V. Hasirci, *Bioact. Mater.* **2018**, *3*, 355.
[46] W. Yang, Y. Qin, Z. Wang, T. Yu, Y. Chen, Z. Ge, *Sens. Actuators, A* **2022**, *333*, 113229.
[47] H. Lai, B. Gong, J. Yin, J. Qian, *Mater. Des.* **2022**, *218*, 110663.
[48] S. V. Murphy, A. Atala, *Nat. Biotechnol.* **2014**, *32*, 773.
[49] M. A. A. Smith, M. I. Khot, S. Taccola, N. R. Fry, P. L. Muhonen, J. L. Tipper, D. G. Jayne, R. W. Kay, R. A. Harris, *Biomed. Microdevices* **2023**, *25*, 16.
[50] S. B. Rauer, D. J. Bell, P. Jain, K. Rahimi, D. Felder, J. Linkhorst, M. Wessling, *Adv. Mater. Technol.* **2022**, *7*, 2100836.
[51] C. Y. Kim, J. H. Myung, J. Y. Sun, W. R. Yu, *Adv. Mater. Technol.* **2023**, *8*, 2300129.
[52] G. Dijk, A. L. Rutz, G. G. Malliaras, *Adv. Mater. Technol.* **2020**, *5*, 1900662.
[53] D. Marrero, A. Guimera, L. Maes, R. Villa, M. Alvarez, X. Illa, *Lab Chip* **2023**, *23*, 1825.
[54] M. Marzocchi, I. Gualandi, M. Calienni, I. Zironi, E. Scavetta, G. Castellani, B. Fraboni, *ACS Appl. Mater. Interfaces* **2015**, *7*, 17993.
[55] N. Jiménez, V. J. D. Krouwer, J. A. Post, *Cytotechnology* **2013**, *65*, 1.
[56] A. S. Zeiger, B. Hinton, K. J. Van Vliet, *Acta Biomater.* **2013**, *9*, 7354.
[57] T. W. Chung, D. Z. Liu, S. Y. Wang, S. S. Wang, *Biomaterials* **2003**, *24*, 4655.
[58] P. M. Van Midwoud, A. Janse, M. T. Merema, G. M. M. Groothuis, E. Verpoorte, *Anal. Chem.* **2012**, *84*, 3938.
[59] K.-H. Nam, N. Jamilpour, E. Mfoumou, F.-Y. Wang, D. D. Zhang, P. K. Wong, *Sci. Rep.* **2014**, *4*, 6965.
[60] D. E. J. Anderson, M. T. Hinds, *Ann. Biomed. Eng.* **2011**, *39*, 2329.
[61] L. Wang, B. Sun, K. S. Ziemer, G. A. Barabino, R. L. Carrier, *J. Biomed. Mater. Res.* **2010**, *93A*, 1260.
[62] Y. Liang, A. Offenhäusser, S. Ingebrandt, D. Mayer, *Adv. Healthcare Mater.* **2021**, *10*, 2100061.
[63] H. Bruus, *Theoretical Microfluidic*, Oxford University Press, Oxford **2006**.
[64] S. H. Chang, C. H. Chiang, F. S. Kao, C. L. Tien, C. G. Wu, *IEEE Photonics J.* **2014**, *6*, 1.
[65] F. M. Smits, *Bell Syst. Tech. J.* **1958**, *37*, 711.